Eur. Phys. J. A **18**, 103–116 (2003)
DOI 10.1140/epja/i2002-10166-9

THE EUROPEAN PHYSICAL JOURNAL A

Fragment charge correlations and spinodal decomposition in finite nuclear systems

G. Tăbăcaru[1,2,a], B. Borderie[1,b], P. Désesquelles[1], M. Pârlog[1,2], M.F. Rivet[1], R. Bougault[3], B. Bouriquet[4], A.M. Buta[3], E. Galichet[1,5], B. Guiot[4], P. Lautesse[6], N. Le Neindre[4,c], L. Manduci[3], E. Rosato[7], B. Tamain[3], M. Vigilante[7], and J.P. Wieleczko[4]

[1] Institut de Physique Nucléaire, IN2P3-CNRS, F-91406 Orsay cedex, France
[2] National Institute for Physics and Nuclear Engineering, RO-76900 Bucharest-Măgurele, Romania
[3] LPC, IN2P3-CNRS, ENSICAEN et Université, F-14050 Caen cedex, France
[4] GANIL, CEA et IN2P3-CNRS, B.P. 5027, F-14076 Caen cedex, France
[5] Conservatoire National des Arts et Métiers, F-75141 Paris cedex 03, France
[6] Institut de Physique Nucléaire, IN2P3-CNRS et Université, F-69622 Villeurbanne cedex, France
[7] Dipartimento di Scienze Fisiche e Sezione INFN, Universitá di Napoli "Federico II", I80126 Napoli, Italy

Received: 22 November 2002 / Revised version: 22 April 2003 /
Published online: 30 September 2003 –
Communicated by D. Guerreau

Abstract. Enhanced production of events with almost equal-sized fragments is experimentally revealed by charge correlations in the multifragmentation of a finite nuclear system selected in ^{129}Xe central collisions on ^{nat}Sn. The evolution of their weight with the incident energy: 32, 39, 45, 50 AMeV, is measured. Dynamical stochastic mean-field simulations performed at 32 AMeV, in which spinodal instabilities are responsible for multifragmentation, exhibit a similar enhancement of this kind of events. The above experimental observation evidences the spinodal decomposition of hot finite nuclear matter as the origin of multifragmentation in the Fermi energy regime.

PACS. 25.70.Pq Multifragment emission and correlations – 24.60.Ky Fluctuation phenomena

1 Introduction

When enough energy is brought into a nucleus, it breaks up into smaller pieces: this is called multifragmentation [1, 2]. The knowledge of this process, experimentally observed for many years, was recently strongly improved with the analysis of experiments performed with powerful detection arrays [3–12]. As a theoretical framework for describing this phenomenon, the analysis of the bulk dynamics of nuclear matter, under various conditions of density and internal energy, has found arguments that multifragmentation occurs when nuclear matter has expanded through the spinodal region of negative compressibility [13]. In this area of mechanical instabilities, covering a large part of a liquid-gas–type coexistence domain, the irreversible growth of local density fluctuations leads the system to the separation into two phases: the spinodal decomposition. For the liquid part primary fragments of nearly equal sizes should be favoured, in relation to the wavelengths of the most unstable modes [14]. Effects like beating of different modes, coalescence of nascent fragments, secondary decay of the excited fragments and, above all, finite-size effects are expected to deeply blur this simple picture [15, 16]. However, evidence for an enhancement of events with nearly equal-sized fragments was for the first time observed in 32 AMeV ^{129}Xe + ^{nat}Sn central collisions leading to a fused system which undergoes multifragmentation, by using a charge correlation method [17]. By means of this model-independent method, recently improved [18], we are investigating here the evolution of the equal-sized fragment partitions with the increase of the incident energy up to 50 AMeV, in selected samples of experimental fused events concerning the same system. In the same framework, for collisions at the lowest energy, the predictions of the 3D stochastic mean-field simulations are successfully compared to the experimental results; these simulations take into account the dynamics of the most unstable modes in the spinodal region.

[a] *Present address*: Cyclotron Institute, Texas A&M University, College station, Texas 77845, USA.
[b] e-mail: borderie@ipno.in2p3.fr
[c] *Permanent address*: Institut de Physique Nucléaire, IN2P3-CNRS, F-91406 Orsay cedex, France.

The paper is organized as follows. In sect. 2 we firstly present the experimental set-up, including the detector array specifications and operating conditions during experiment. Secondly, we recall the criteria allowing to select the experimental events corresponding to fused systems in central collisions. The general features of the related experimental data are evidenced in sect. 3. In sect. 4, the charge correlation method with some improvements and developments is described; results of stochastic mean-field simulations are used to exemplify and to compare the potentiality of the up-dated version to the original method. The experimental results, obtained at different incident energies, are then shown; they are discussed and interpreted in sect. 5. Conclusions of this study are drawn in sect. 6.

2 Experimental selection of a finite piece of nuclear matter

Heavy-ion collisions at relative velocities comparable to those of the nucleons in the nucleus may provide test pieces of nuclear matter at moderate temperatures which are good candidates to undergo a nuclear liquid-gas–type phase transition. Indeed, "fused" systems reaching sizes up to a few hundred nucleons may be obtained in the laboratory, by colliding accelerated heavy projectiles with heavy targets. By means of 4π detection arrays of high granularity, it is possible to completely study their disassembly. Such events are expected to appear with high probability for central collisions, but one major problem is to select them among reactions with a dominant binary character [19].

2.1 Experimental procedure

The ^{129}Xe + ^{nat}Sn system was studied with the 4π multidetector INDRA, operating at the GANIL accelerator. A thin target of natural tin ($350\,\mu$g/cm^2) was bombarded by ^{129}Xe projectiles at five incident energies: 25, 32, 39, 45 and 50 AMeV. Low-intensity beams ($\sim 3 \times 10^7$ pps) were used to keep the random coincidence rate below 10^{-4}. The low target thickness allows slow fragments to escape the target. A trigger based on the multiplicity was chosen, requiring at least four modules firing. In the off-line analysis, events having a multiplicity of correctly identified charged particles inferior to the experimental trigger condition were rejected for reasons of coherency. The most peripheral collisions are thus eliminated.

INDRA, which is described in detail in [20,21], can be viewed as an ensemble of 336 telescopes covering about 90% of the 4π solid angle. The detection cells are distributed amongst 17 rings centred on the beam axis. Low-energy identification thresholds (from $\approx$ 0.7 AMeV for $Z = 3$ to $\approx$ 1.7 AMeV for $Z = 50$) and large energy ranges were obtained through the design of three layer telescopes, composed of an axial-field ionization chamber operated at 30 mbar of C_3F_8, a 300 μm silicon detector and a CsI(Tl) scintillator, thick enough to stop all emitted particles, coupled to a phototube. Such a telescope can detect and identify from protons between 1 and 200 MeV to uranium ions of 4 GeV. Past 45°, where fast projectile-like fragments are no longer expected, the telescopes comprise only two stages, the ionization chamber operated at 20 mbar and the scintillator. Finally, the very forward angles (2–3°) are occupied by NE102-NE115 phoswiches.

A charge resolution of one unit was obtained for the whole range of atomic number of fragments identified through the $\Delta E - E$ method in the Si-CsI(Tl) couple. For CsI(Tl) scintillators, a better understanding of the light response was obtained and the contribution of δ-rays generated by the incoming heavy ion was taken into account [22]. A direct consequence was the identification of fragments with a resolution of one charge unit up to $Z = 20$, and a few charge units for the heaviest fragments, in ionization chamber-CsI(Tl) telescopes [23]. The exact identification of fragments up to at least $Z = 20$ reveals itself to be essential for the charge correlation studies which are the aim of this paper.

2.2 Selection of single-source events

A two-step procedure has been used to isolate fused systems. The first step was to keep the events for which a quasi-complete detection of the reaction products has been achieved. Significant fractions, $\geq 77\%$ of the charge of the system, $Z_{sys} = Z_{proj} + Z_{targ}$, and $\geq 75\%$ of the beam momentum, P_{proj}, in the exit channel were required to be measured for every event. INDRA does not permit isotopic identification for fragments and does not detect the neutrons. For this reason, the momentum used here is calculated from the product of the atomic number Z and the velocity component in the beam direction v_z: $P_{tot} = \Sigma Z v_z$ and normalized to the incident (projectile) momentum: $Z_{proj} v_{proj}$. In the second step we used the flow angle (Θ_{flow}) selection [24,25,19]. This global variable is defined as the angle between the beam axis and the preferred direction of emitted matter in each event. It is determined by the energy tensor calculated from fragment ($Z \geq 5$) momenta in the reaction centre of mass. Fused events have no memory of the entrance channel and should be isotropic while binary dissipative collisions are focused at small Θ_{flow}. Thus, by selecting only large flow angles, fused events can be well isolated. In [19] the minimum flow angle chosen for 32 AMeV collisions was 70°. It was 60° for 50 AMeV collisions [26]. In this paper we chose 60° for all energies, to get enough statistics (at least 30000 events) without degrading the properties of a compact fused source.

The present selection corresponds to measured cross-sections decreasing from 56 to 19 mb when the incident energy goes from 25 to 50 AMeV (see table 1). By taking into account detection efficiency and biases due to the selection (quasi-complete events and flow angle selection) the total cross-section for the formation of compact fused systems is estimated to decrease from 250 to 85 mb between 25 and 50 AMeV [27].

Table 1. Exit channel average values of the total and fragment ($Z \geq 5$) multiplicity, total charge emitted in fragments and fragment atomic number, in events from ^{129}Xe + $^{\rm nat}$Sn central collisions, as functions of the entrance channel characteristics: incident and available energy. The numbers in parentheses are the standard deviations of the distributions. The measured cross-sections are given in the last column.

E AMeV	$E_{\rm cm}/A_{\rm sys}$ AMeV	$\langle M_{\rm tot}\rangle$	$\langle M_{\rm f}\rangle$	$\langle Z_{\rm bound}\rangle$	$\langle Z_{\rm f}\rangle$	$\sigma_{\rm meas.}$ mb
25	6.24	18.9 (2.7)	3.56 (1.04)	67.3 (6.8)	17.6	$56. \pm 8.$
32	7.99	23.8 (3.0)	4.13 (1.17)	57.6 (7.0)	13.4	$26. \pm 4.$
39	9.73	28.5 (3.1)	4.41 (1.20)	49.6 (7.4)	11.0	$18. \pm 3.$
45	11.23	31.5 (3.3)	4.42 (1.19)	44.0 (7.5)	9.7	$19. \pm 5.$
50	12.48	34.2 (3.3)	4.31 (1.18)	39.7 (7.6)	9.0	$19. \pm 3.$

3 Global properties of selected fused events

Before presenting and discussing charge correlations, which deal with information inside events, it is useful to have an overview of the related inclusive properties of the selected events, like the multiplicity and charge distributions. Entrance channel conditions for the Xe + Sn system of total mass $A_{\rm sys} = 248$ and charge $Z_{\rm sys} = 104$ are summarized in table 1.

3.1 Multiplicity and bound charge

Figure 1 shows multiplicity and total charge ($Z_{\rm bound} = \sum_{Z \geq Z_{\rm min}} Z$) distributions normalized to the number of events, at the five incident energies. The total multiplicity distributions, when all the charged reaction products are considered, $Z \geq 1$, are shown in fig. 1a). They all display a Gaussian shape; the most probable multiplicity values and the standard deviations increase with the available energy, as shown in table 1. At 50 AMeV the average multiplicity reaches one third of the total charge. The distributions of the sum of the charges of all the reaction products, plotted in fig. 1e), for different energies, are practically identical, nicely testifying about the negligible variation of the detection efficiency of INDRA when the incident energy significantly varies. The common limitation at 80 charge units is demanded by the software as a criterion for the completeness of event detection. These two plots, considered together, speak about the increasing number of reaction products from central collisions with the incident energy.

The evolution of the reaction product multiplicity distribution, at all energies, when another lower charge limit is imposed, is presented afterwards in the left column of the same figure. As compared to fig. 1a) ($Z \geq 1$), the splitting of the energy-dependent distributions is diminishing if $Z \geq 3$ (fig. 1b); the curves become completely superimposable, except at 25 AMeV, for $Z \geq 5$ (fig. 1c) and split again, but in the opposite sense, if $Z \geq 8$ (fig. 1d). De-excitation simulations for primary fragments having the same N/Z ratio as the total system, performed by means of the statistical code SIMON [28] at 3 AMeV excitation energies, have indicated small evaporation rates of Li and Be isotopes, but negligible rates of heavier nuclei [29]. This average value of 3 AMeV for the fragment excitation energy was deduced from fragment-particle correlations for the same system between 32 and 50 AMeV incident energy [30,27]. Moreover the daughter nucleus atomic number is, on average, one charge unit smaller than that of the parent fragment, with a standard deviation of about one unit. It may be thus inferred that the distribution of the number of primary fragments with $Z \geq 5$ is not dramatically modified by the secondary decay. More precisely, as indicated in table 1, the average number of fragments with $Z \geq 5$ reaches a maximum for an incident energy as low as 39 AMeV and starts decreasing above 45 AMeV.

If the lower limit is set to $Z_{\rm min} = 3$, for comparison with other works, the maximum value, 7.1 fragments, is reached at 50 AMeV. The same maximum value is obtained for the asymmetric Ni + Au collisions measured with INDRA [31]. These results can be compared with a series of measurements of fragment multiplicities published in [32]. Using for the present data a similar selection method would increase the INDRA value by $\sim 10\%$. These INDRA data, combined with those related to Ni + Ni and Kr + Nb of [32] show that the maximum average number of fragments produced in central collisions (multifragmentation) is proportional to the total system mass $A_{\rm sys}$ up to at least $A_{\rm sys} \sim 250$; there is no indication of a saturation, as inferred from the Kr + Au data of [33] and from percolation calculations. The maximum number of fragments for $A_{\rm sys} \sim 250$ is moreover reached for a c.m. available energy of ~ 12 AMeV in the INDRA measurements, much lower than those quoted in [32].

Panels f), g), h) in the right column of fig. 1 show the distributions of the sum of the charges of the reaction products having atomic numbers $Z \geq 3$, 5, and 8, respectively. The independence of the energy, seen in fig. 1e), is progressively removed from top to bottom and the populated domain shifts towards lower values of the total charge of the reaction products taken into account. For $Z \geq 5$, for example, the shapes of the distribution are very alike: Gaussians which are slightly broadening with increasing energy, but centred at lower and lower values of the sum $Z_{\rm bound}$ of the fragment charges. For $Z \geq 8$ and the largest incident energies (45 and 50 AMeV) shoulders are observed at low $Z_{\rm bound}$, which indicates the onset of events with a high degree of fragmentation: those events have only one fragment with a charge in the range 8–14.

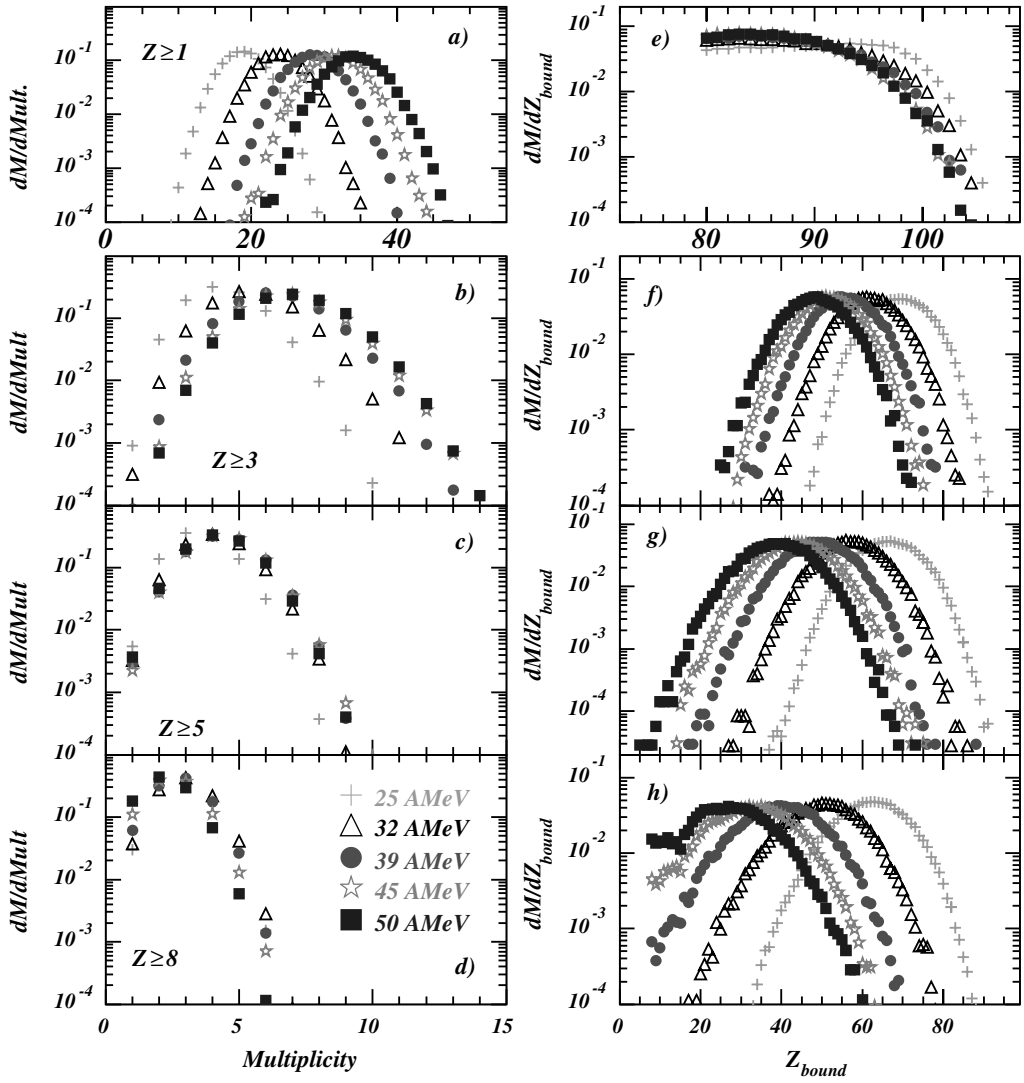

Fig. 1. Experimental multiplicity (left) and total charge (right) distributions for the selected events from central 25, 32, 39, 45 and 50 AMeV ^{129}Xe + $^{\rm nat}$Sn collisions, with different lower thresholds $Z_{\rm min}$ for the reaction products taken into account. From top to bottom: $Z_{\rm min}$ = 1, 3, 5, 8. Note that panel e) thus displays the total detected charge.

The evolution of the exit channel average measured quantities with the available energy is also synthesized in table 1. These average values concern: the total multiplicity, $M_{\rm tot}$, the fragment ($Z \geq 5$) multiplicity, $M_{\rm f}$, the total charge emitted in fragments, $Z_{\rm bound}$, and the fragment atomic number, $Z_{\rm f}$. The growth of the average total multiplicity, when the incident energy increases, is accounted for by the growth of the light nuclei ($Z \leq 4$) average multiplicities, while the average fragment multiplicity barely changes. The ratio of the bound charge to the total charge of the system goes down with increasing excitation energy. The size of the produced fragments is diminishing too, as a proof that the collisions are becoming more violent. At a given incident energy, however, $Z_{\rm bound}$ increases roughly linearly as a function of fragment ($Z \geq 5$) multiplicity with a slope varying from 3 to 4.5 when the energy increases from 25 to 50 AMeV. This again indicates that at higher energy the system is highly fragmented.

3.2 Charge distributions

The charge distributions, normalized to the number of single-source events, can be compared all together in fig. 2. When the available energy increases, the emission of small fragments ($Z < 10$) increases while that of fragments with $Z > 15$ decreases producing steeper and steeper distributions; quite equivalent rates of production for fragments with $10 \leq Z \leq 15$ are observed between 32 and 50 AMeV. The domain of the heaviest fragments $Z \approx 50$, populated at the lowest energy, gradually vanishes at higher energies. This behaviour is quite remarkable, particularly seeing that the number of fragments is the same at all energies (fig. 1c). Roughly, one observes the following trend: the curves are gradually passing from a regime with two slopes, at the lowest incident energy, towards a regime with one slope, at the highest incident energy. The average measured charge of the fragments can be found in table 1.

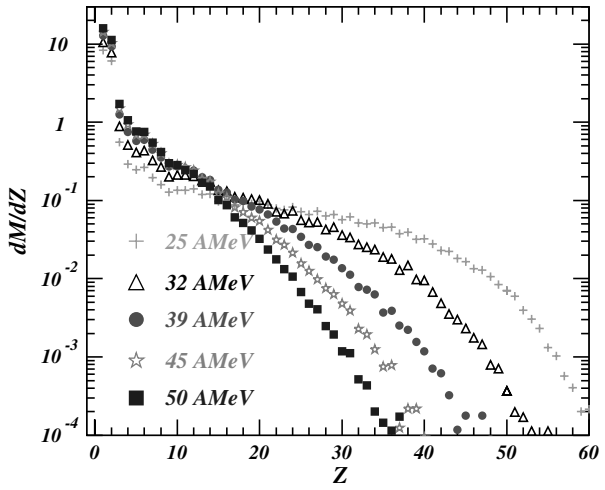

Fig. 2. Experimental differential charge multiplicity distributions for the selected events formed in central 25, 32, 39, 45 and 50 AMeV ^{129}Xe + $^{\rm nat}$Sn collisions.

4 Charge correlation functions and enhanced production of nearly equal-sized fragment events

A few years ago a new method called higher-order charge correlations [34] was proposed to enlighten any extra production of events with specific fragment partitions. The high sensitivity of the method makes it particularly appropriate to look for small numbers of events as those expected to have kept a memory of spinodal decomposition properties. Thus, such a charge correlation method allows to examine model-independent signatures that would indicate a preferred decay into a number of equal-sized fragments in events from experimental data or from simulations. In this section and the following only events with 3 to 6 fragments ($Z \geq 5$) at 32, 39, 45 and 50 AMeV will be considered. They represent in all cases 90–92% of the selection previously considered. At these four energies, the detection efficiency is independent of the fragment charge, in the selected event samples. This is not so well verified at 25 AMeV.

4.1 Methods

The classical two-fragment charge correlation method considers the coincidence yield $Y(Z_1, Z_2)$ of two fragments of atomic numbers $Z_{1,2}$, in the events of multiplicity $M_{\rm f}$ of a sample. A background yield $Y'(Z_1, Z_2)$ is constructed by mixing, at random, fragments from different coincidence events selected by the same cut on $M_{\rm f}$. The two-particle correlation function is given by the ratio of these yields. When searching for enhanced production of events which break into equal-sized fragments, the higher-order correlation method appears much more sensitive. All fragments of one event with fragment multiplicity $M_{\rm f} = M = \sum_Z n_Z$, where n_Z is the number of fragments with charge Z in the partition, are taken into account. By means of the normalized first-order,

$$\langle Z \rangle = \frac{1}{M} \sum_Z n_Z Z \tag{1}$$

and second-order,

$$\sigma_Z^2 = \frac{1}{M} \sum_Z n_Z (Z - \langle Z \rangle)^2, \tag{2}$$

moments of the fragment charge distribution in the event, one may define the higher-order charge correlation function:

$$1 + R(\sigma_Z, \langle Z \rangle) = \left. \frac{Y(\sigma_Z, \langle Z \rangle)}{Y'(\sigma_Z, \langle Z \rangle)} \right|_M . \tag{3}$$

Here, the numerator $Y(\sigma_Z, \langle Z \rangle)$ is the yield of events with given $\langle Z \rangle$ and σ_Z values. Because the measurement of the charge belonging to a given event is not subject to statistical fluctuations, we use here expression (2) rather than the "nonbiased estimator" of the variance, $\frac{1}{M-1} \sum_Z n_Z (Z - \langle Z \rangle)^2$, as proposed in [34] and used in our previous paper [17]. Note that this choice has no qualitative influence on the forthcoming conclusions. The denominator $Y'(\sigma_Z, \langle Z \rangle)$, which represents the uncorrelated yield of pseudo-events, was built in [34], as for classical correlation methods, by taking fragments at random in different events of the selected sample of a certain fragment multiplicity. This Monte Carlo generation of the denominator $Y'(\sigma_Z, \langle Z \rangle)$ can be replaced by a fast algebraic calculation which is equivalent to the sampling of an infinite number of pseudo-events [18]. Its contribution to the statistical error of the correlation function is thus eliminated. However, owing to the way the denominator was constructed, only the fragment charge distribution $\mathrm{d}M/\mathrm{d}Z$ of the parent sample is reproduced but the constraints imposed by charge conservation are not taken into account. This has, in particular, a strong effect on the charge bound in fragments $\mathrm{d}M/\mathrm{d}Z_{\rm bound}$ distribution. This fact makes the denominator yield distributions as a function of $\langle Z \rangle$ wider and flatter than those of the numerator [29]. Consequently, even in the absence of a physical correlation signal, the ratio (3) is not a constant equal to one. The correlations induced by the finite size of the system (charge conservation) distorts the amplitude, or even may cancel other less trivial correlations. Therefore, a new method for the evaluation of the denominator [18], based on the "intrinsic probability" of emission of a given charge, was adopted. It minimizes these effects and replicates all features of the partitions of the numerator, except those (of interest) due to other reasons than charge conservation.

The goal of the method is to take into account in a combinatorial way the trivial correlations due to charge conservation. If there is no correlation between the charges, each charge can be fully described by an emission probability (referred to as intrinsic probability

and noted ${}^{\rm intr}P_Z$). This fact was largely demonstrated for the bulk of multifragment emission around the Fermi energy [35]. Without charge conservation constraint, the intrinsic probabilities would be equal to the emission probability. Charge conservation makes the emission probability of high-charge fragments smaller than their intrinsic probability, whereas it is the contrary for small charges. The probability to observe a given partition $(\mathbf{n} : (n_1, \ldots, n_{Z_{\rm tot}}))$, at a given total multiplicity, $M_{\rm tot} = m = \sum_Z n_Z$, is obtained by the multinomial formula. If the total charge is fixed ($Z_{\rm tot} = \sum_Z Z n_Z$), the partition probabilities are given by

$$P(\mathbf{n} \mid m) = \alpha m! \prod_Z \frac{{}^{\rm intr}P_Z^{n_Z}}{n_Z!} \delta_{Z_{\rm tot}, \sum_Z Z n_Z}, \qquad (4)$$

where α is the normalization constant (so that $\sum_n P(\mathbf{n} \mid m) = 1$) and δ is the Kronecker symbol. For the reason previously mentioned, no Z-dependent efficiency term is needed in this formula. These partition probabilities contain all information relative to the charges and their correlations. For example, the denominator $Y'(\sigma_Z, \langle Z \rangle)$ is obtained by summing the probabilities of the partitions with given mean charge and standard deviation. Of course, the intrinsic probabilities are not direct experimental observables, they have to be evaluated by inversion of eq. (4). However, *this inversion is possible only if the physical correlations* (not due to charge conservation) *are weak*. If the data sample contains only trivial correlations, then the higher-order charge correlation function (or any other correlation function) is everywhere equal to 1. Local positive (negative) physical correlations will appear as peaks (holes). In the case of experimental events, it has to be noted that a set of intrinsic probabilities exists only if the selected sample comprises essentially single-source events having reached thermal equilibrium (the source has to be described by a unique set of intrinsic probabilities). Otherwise, the results would be equal to the convolution of the partition probabilities corresponding to the different source sizes, each of them being described by a different set of intrinsic probabilities. Hence, the convergence of the inversion procedure (eq. (4)) is a strong indication that these two conditions are fulfilled by the sample under study [18]. The data samples correspond to multifragmenting single sources, supplemented by pre-equilibrium and secondary decay particles and light fragments. Hence, only fragments with charge greater than or equal to 5 have been retained for the analysis of the multifragmenting source. This feature has to be taken into account in the calculation of the denominator. The fragment partition $(\mathbf{N} : (n_5, \ldots, n_{Z_{\rm tot}}))$ probability can be calculated as the sum over the complete partitions $\mathbf{n}$ which include $\mathbf{N}$. Denoting by M the fragment multiplicity, it can be straightforwardly shown from eq. (4) that the fragment partition probability reads

$$P(\mathbf{N}) = f(M, Z_{\rm bound}) P'(\mathbf{N}), \qquad (5)$$

with

$$f(M, Z_{\rm bound}) = \alpha \sum_{\mathbf{n}:(n_1,\ldots,n_4)} \binom{m}{M} (m - M)! \times \prod_{Z=1}^{4} \frac{{}^{\rm intr}P_Z^{n_Z}}{n_Z!} \delta_{Z_{\rm tot} - Z_{\rm bound}, \sum_{Z=1}^{4} Z n_Z},$$

$$P'(\mathbf{N}) = M! \prod_{Z=5}^{Z_{\rm tot}} \frac{{}^{\rm intr}P_Z^{n_Z}}{n_Z!}, \qquad (6)$$

where $\binom{m}{M}$ are the binomial coefficients. The value of $Z_{\rm tot}$ was fixed at the total charge of the system, $Z_{\rm projectile} + Z_{\rm target}$; it has been noticed that, whereas the total charge conservation has to be explicitly included in the calculation, the results are only modified when $Z_{\rm tot}$ is lower than 85. This new method to build the denominator will be denoted as the Intrinsic Probability Method (IPM) in what follows. However, the explicit calculation of the intrinsic probabilities may not be the only method for building a denominator including only the correlations induced by charge conservation (another procedure is proposed in [36], see the appendix for a comparison with the IPM method). In any case, by definition, all valid methods lead to a partition probability described by eq. (4).

A comparison of the results obtained in the framework of the higher-order correlation method, with the analytical denominator, and with IPM, will be drawn in the following for an event sample resulting from a simulation of 32 AMeV ^{129}Xe + ^{119}Sn central collisions.

4.2 Stochastic mean-field and spinodal decomposition

Dynamical stochastic mean-field simulations have been proposed for a long time to describe processes involving instabilities like those leading to spinodal decomposition [37–39]. In this approach, spinodal decomposition of hot and dilute finite nuclear systems can be mimicked through the Brownian One-Body (BOB) dynamics [40, 41,7], which consists in employing a Brownian force in the kinetic equations. Simulations have been performed for head-on ^{129}Xe on ^{119}Sn collisions at 32 AMeV. The ingredients of simulations can be found in [7] as well as a detailed comparison between filtered simulated events (to account for the experimental device) and experimental data. A good agreement between both is revealed.

To refine the comparison higher-order charge correlations have been calculated for the simulated events, keeping the compact presentation proposed in [17]: charge correlation functions are built for all events, whatever their multiplicity, by summing the correlated yields for all M and by replacing the variable $\langle Z \rangle$ by $Z_{\rm bound} = M \times \langle Z \rangle = \sum_Z Z n_Z$. Uncorrelated events are constructed and weighted in proportion to real events of each multiplicity. This presentation is based on the experimental observation that the peaks observed independently for each fragment multiplicity correspond

to the same $Z_{\rm bound}$ region [17]. The variance bin was chosen equal to one charge unit. We recall that in the considered domain of excitation energy, around 3 MeV per nucleon [30,7], secondary evaporation leads to fragments one charge unit smaller, on average, than the primary $Z \approx 10$–20 ones, with a standard deviation around one [29]. If a weak enhanced production of exactly equal-sized fragments exists, peaks are expected to appear in the interval $\sigma_Z = 0$–1, because of secondary evaporation. This interval in σ_Z is hence the *minimum* value which must be chosen to look for nearly equal-sized fragments. Any (unknown) intrinsic spread in the fragment size coming from the break-up process itself may enlarge the σ_Z interval of interest. This will be discussed at the end of the section, for the moment we will consider only events with $\sigma_Z < 1$, which corresponds to differences of at most two units between the fragment atomic numbers in one event.

Figure 3 shows the correlation function calculated using the analytical denominator (a) or the denominator given by the IPM (b). Both functions are drawn *versus* the variables $Z_{\rm bound} = M \times \langle Z \rangle$ and σ_Z. In fig. 3a, the equal-sized fragment correlations in the first bin are superimposed over trivial correlations due to the finite size of the system. For this reason, the ratio (3) is generally different from one and smoothly varies with the variables $Z_{\rm bound}$ and σ_Z. For each bin in $Z_{\rm bound}$ (fixed at 6 atomic number units), an exponential evolution of the correlation function is observed from $\sigma_Z = 7$–8 down to $\sigma_Z = 2$–3. This exponential evolution is thus taken as a "background" empirically extrapolated down to the first bin $\sigma_Z = 0$–1. The amplitude of the correlation function in the domain $Z_{\rm bound} =$ 36–60 is well above the background, with a confidence level higher than 90%, proving thus a statistically significant enhancement of equal-sized fragment partitions. Of the 1% of events having $\sigma_Z < 1$, (0.13 ± 0.02)% (called extra events from now on) are in excess of the background. In fig. 3b, as expected, all correlations due to the charge conservation are suppressed and the correlation function is equal to 1 (within statistical fluctuations) wherever no additional correlation is present. Again one observes peaks for $\sigma_Z < 1$. The percentage of extra events is 0.36 ± 0.03%, higher than the one obtained with the previous method. Moreover, with this method, peaks also appear at the maximum values of σ_Z for a given $Z_{\rm bound}$. They correspond to events composed of one big (a heavy residue) and several lighter fragments (sequentially emitted from the big one). In that case fusion-multifragmention does not occur and the peaks reveal the small proportion (0.15%) of events which undergo the fusion-evaporation process. The IPM approach may thus reveal other correlations not seen with the previous one. Therefore, we shall use this approach in the following analysis of the experimental data.

To conclude this part we can say that, although all events in the simulation arise from spinodal decomposition, only a very small fraction of the final partitions have nearly equal-sized fragments. Different effects: beating of different modes, coalescence of nascent fragments, secondary decay of the excited fragments and, above all, finite-size effects are responsible for this fact [15,16]. The signature of spinodal decomposition can only reveal itself as a "fossil" signal.

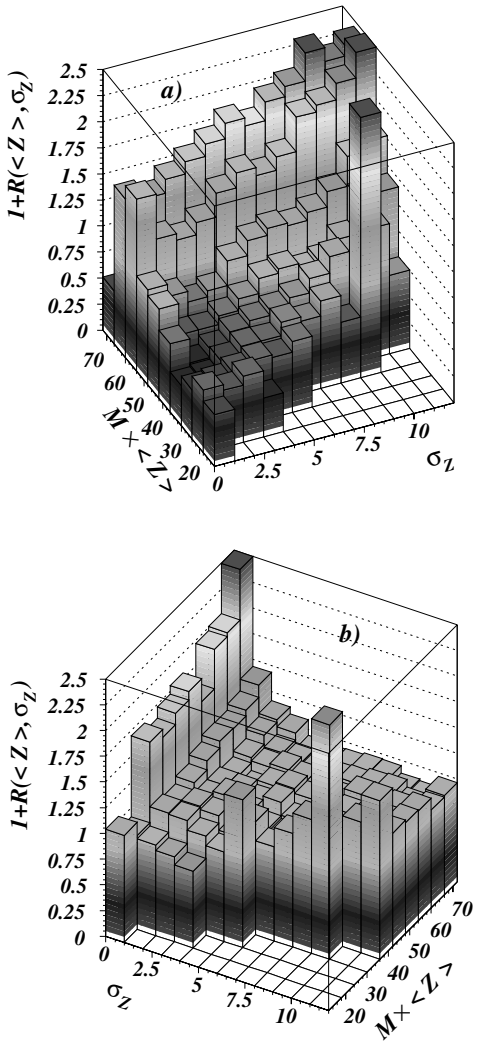

Fig. 3. Correlation functions for events with $M_{\rm f} = 3$ to 6, simulated with the Brownian One-Body model for 32 AMeV ^{129}Xe + $^{\rm nat}$Sn collisions. a) With an analytical denominator provided by pseudo-events; b) with a denominator calculated with the IPM. The orientations of a) and b) are different for a better visualisation of the landscapes.

4.3 Experimental results

We shall present now higher-order charge correlations for the selected experimental events. This will be done for four incident energies (32, 39, 45 and 50 AMeV) in the framework of the IPM for the denominator. The first step consists in determining the intrinsic probabilities of fragments for each multiplicity and at each incident energy. These probabilities are obtained by a recursive procedure of minimization. The minimization criterion is the normalized χ^2 between the experimental fragment probabilities and the fragment partition probabilities given by (5). The calculated χ^2 were always lower than one: the lower is the

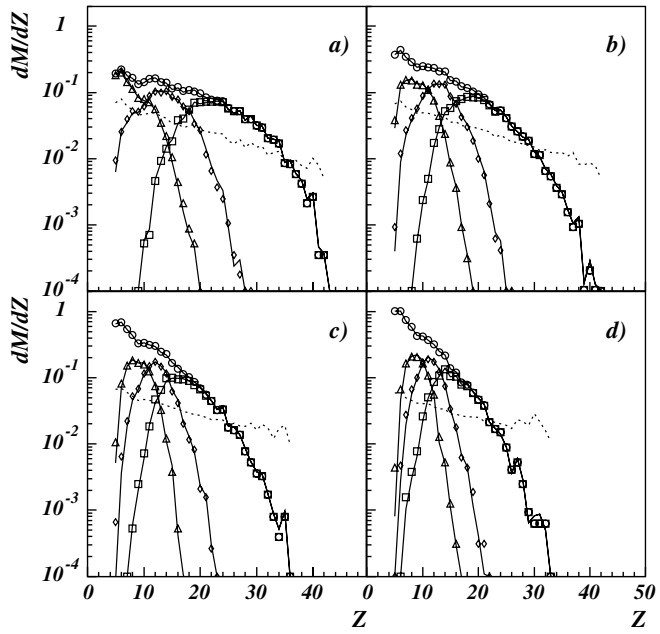

Fig. 4. Experimental differential charge multiplicity distributions (circles) for the single source formed in central 39 AMeV ^{129}Xe on ^{nat}Sn collisions. Parts a, b, c and d refer, respectively, to fragment multiplicities 3, 4, 5, 6. The Z distributions for the first (squares), second (diamonds) and third (triangles) heaviest fragments are presented too. The full lines correspond to the results obtained with IPM. The dashed lines display the intrinsic probabilities.

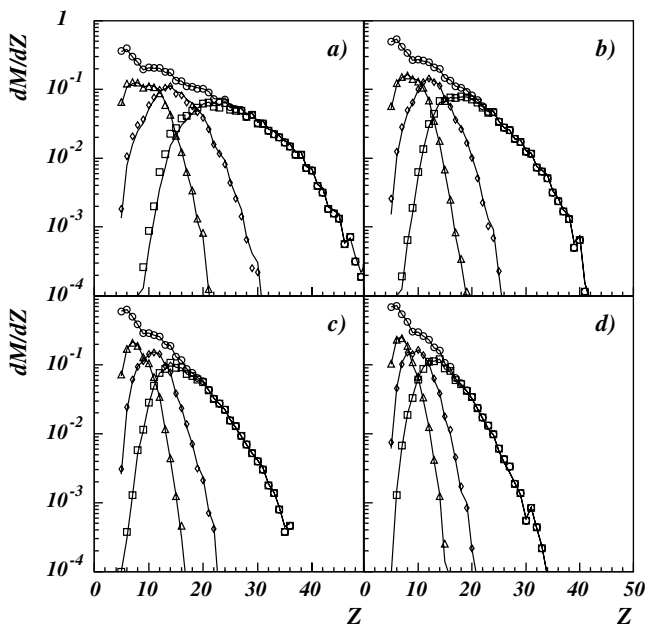

Fig. 5. Experimental differential charge multiplicity distributions (circles) for the single sources formed in central 32, 39, 45 and 50 AMeV ^{129}Xe on ^{nat}Sn collisions (a, b, c, d). The Z distributions for the first (squares), second (diamonds) and third (triangles) heaviest fragments are presented too. The lines correspond to the results obtained with IPM.

incident energy and the larger is the multiplicity, the lower is the χ^2 value.

Charge distributions experimentally observed for the different fragment multiplicities are shown as an example in fig. 4; they correspond to the 39 AMeV incident energy. Dashed lines refer to the intrinsic probabilities calculated with IPM and the corresponding charge distributions are the full lines. The experimental charge distributions are faithfully described. Note that the ratio of the experimental to the calculated curves does not reveal any anomalous enhancement in a preferential domain of fragment atomic number. The charge distributions, summed over fragment multiplicities 3 to 6, are displayed in fig. 5, for the four incident energies. For each incident energy the intrinsic probabilities have been calculated independently for the different fragment multiplicities (see fig. 4) and weighted in proportion to real events of each fragment multiplicity. The slight differences for the intrinsic probabilities corresponding to the different multiplicities reveal small differences in the average excitation energies of the multifragmenting sources (on the other hand, it has been possible to fit all events from the BOB simulation, irrespective of their multiplicity, using the same intrinsic probability distribution due to the fact that the events correspond to the same initial conditions). We note again the excellent agreement between calculations and data at all incident energies. The contributions to the Z distribution of the three heaviest fragments of each partition are as well described as in fig. 4, and the charges bound in fragments (not shown) are also perfectly reproduced.

Figure 6 illustrates the higher-order correlation functions measured for the different fragment multiplicities. It concerns single sources selected at 39 AMeV incident energy. To make the effects more visible, peaks with confidence level lower than 80% were flattened out. We observe significant peaks in the bin $\sigma = 0$–1 for each fragment multiplicity. For $M = 6$, peaks are essentially located in the bin $\sigma_Z = 1$–2. As observed in simulations, peaks corresponding to events composed of a heavy residue and light fragments (σ_Z in the region 5–10 associated with low $\langle Z \rangle$) are also visible.

Let us now present the results for the different incident energies, summed over multiplicities 3–6. We recall again that IPM denominators of correlation functions are weighted in proportion to real events of each multiplicity. In fig. 7 the measured functions are displayed. If we exclude some peaks with low confidence levels (as done in fig. 8) correlation functions are equal or close to one except at low σ_Z values. A summary of average-charge domains contributing to the correlation peaks in the first bin in σ_Z is given in table 2 as a function of fragment multiplicity. All multiplicities, associated to the largest $\langle Z \rangle$ ranges (20–6 and 18–6) contribute to the peaks at 39 and 45 AMeV. At 32 AMeV, the peaks only come from the low multiplicites ($M = 3$–4), with a smaller $\langle Z \rangle$ range: 21–11; at 50 AMeV, the situation is completely different and we only observe a contribution from $M = 6$ with $\langle Z \rangle = 7$–9. Except in this latter case, the $\langle Z \rangle$ domains for

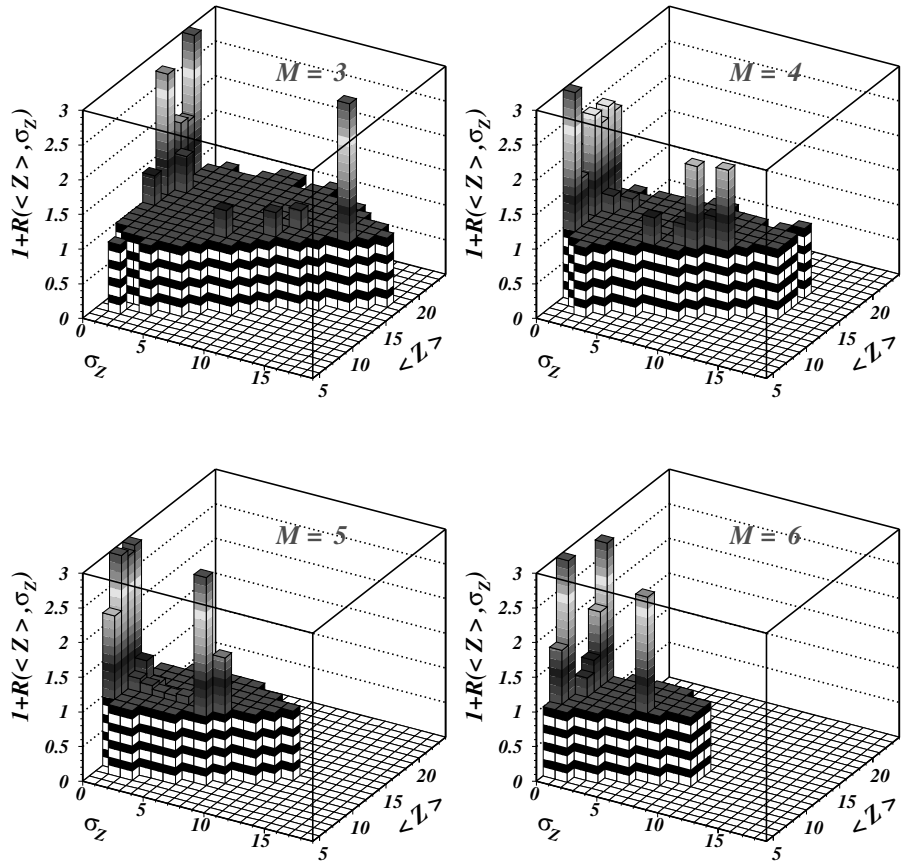

Fig. 6. Experimental higher-order charge correlations for selected events formed in central 39 AMeV ^{129}Xe on $^{\rm nat}$Sn collisions, for fragment multiplicities 3 to 6. The maximum value of the scale of the correlation function is limited to 3 on the picture.

Table 2. Characteristics of events with $\sigma_Z < 1$ for the different incident energies. For each fragment multiplicity M, the range of $\langle Z \rangle$ contributing to the correlation peaks are indicated (for bold $\langle Z \rangle$ ranges, see text). The first line refers to BOB simulations (see sect. 4.2).

M	3	4	5	6
E (AMeV)				
32∗	**12–20**	9–17	8–13	–
32	**13–21**	11–16	–	–
39	**15–20**	8–15	7–11	6–8
45	**17–18**	5–14	8–11	6–8
50	–	–	–	7–9

which correlation peaks are present are similar but slightly shifted towards lower values with increasing energy.

To be quantitative, correlation functions for the first bin in σ_Z are displayed in fig. 9 with their statistical errors. Full points (open points) correspond to a confidence level higher (lower) than 90%. Two percentages of events relatively to the single-source events ($M_{\rm f} = 3$–6) are presented in columns 2 and 3 of table 3: they refer to the total number of events and of extra events (taking into account correlations and anti-correlations) in the bin. The present analysis fully confirms at 32 AMeV incident energy the previous one [17] and the extra-percentage of events with nearly equal-sized fragments is maximum at 39 AMeV.

A closer examination of figs. 3b and 8 reveals an islet of peaks, with a high confidence level, in the second and the third bins in σ_Z. They are located in the upper region of the $M \times \langle Z \rangle$ ranges indicated in table 2. They correspond to events with a broader spread of charges. Observing such events in the simulation may indicate that the intrinsic spread (which is unknown) due to spinodal decomposition is larger than that coming from secondary evaporation, and hence that these peaks also sign the original process. The percentages of events with $\sigma_Z < 3$ are also reported in table 3. The conclusions are the same as above: while more events have small values of σ_Z when the incident energy increases, the percentage of extra events shows a maximum at 39 AMeV, and vanishes at 50 AMeV.

5 Discussion

The first hint of a bulk effect for producing fragments in central collisions between heavy nuclei at a given moderate excitation energy ($\epsilon^* \approx 7$ AMeV) was the measurement of identical fragment charge distributions for two different system sizes (32 AMeV ^{129}Xe + $^{\rm nat}$Sn and 36 AMeV ^{155}Gd + $^{\rm nat}$U) [42]. However, this feature could as well be interpreted from a statistical point of view, namely the

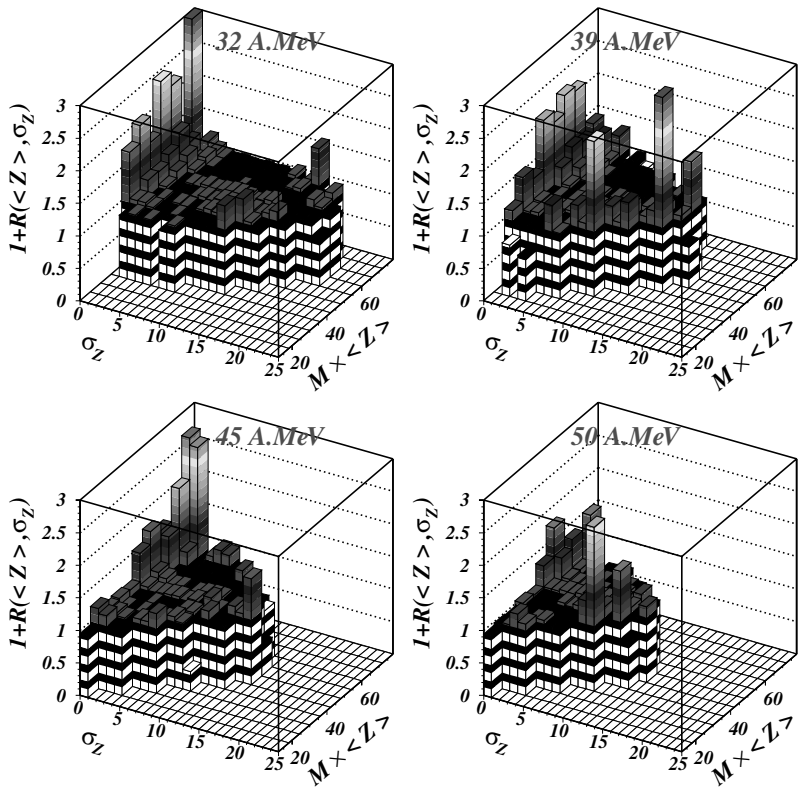

Fig. 7. Experimental higher-order charge correlations for selected events formed in central ^{129}Xe and ^{nat}Sn collisions. Events with $M_f = 3$ to 6 are mixed.

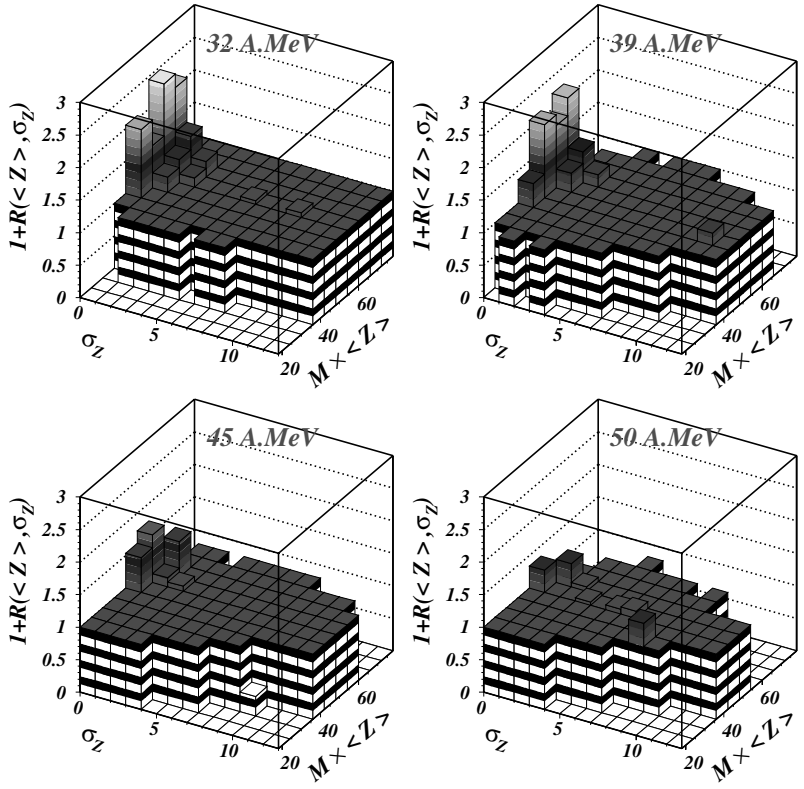

Fig. 8. Same as fig. 7 but peaks (or holes) with a confidence level lower than 90% (1.65 σ) have been flattened out.

Table 3. Numbers and percentages of events for $\sigma_Z < 1$ and $\sigma_Z < 3$ and percentages of extra events. The percentages are expressed with respect to the total number of selected events with fragment multiplicities 3 to 6. The first line refers to simulations (see sect. 4.2).

E	$\sigma_Z < 1$			$\sigma_Z < 3$		
	events		extra events	events		extra events
(AMeV)		(%)	(%)		(%)	(%)
32∗	353	1.0	0.36 ± 0.03	4873	14.0	1.30 ± 0.06
32	83	0.26	0.13 ± 0.02	1746	5.5	0.79 ± 0.05
39	151	0.58	0.25 ± 0.03	4275	16.3	1.29 ± 0.07
45	317	1.32	0.21 ± 0.03	7328	30.6	0.79 ± 0.05
50	762	2.78	0.08 ± 0.02	12306	45	0

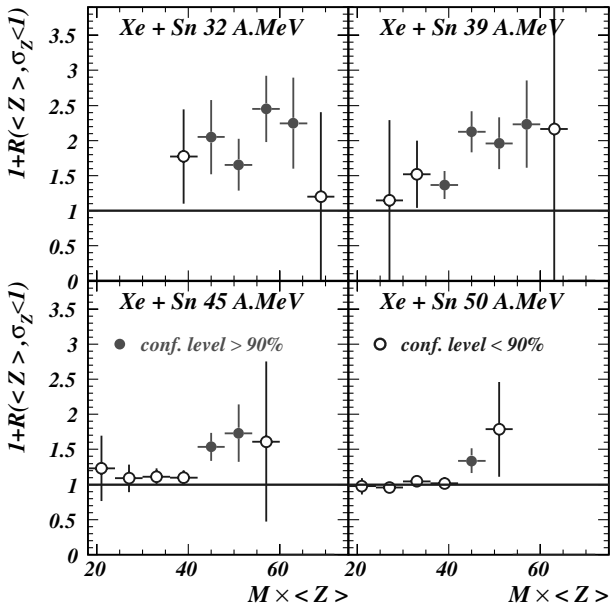

Fig. 9. Higher-order charge correlations at the different incident energies: quantitative results for events with $\sigma_Z < 1$. Errors are statistical assuming independent measurements and horizontal bars correspond to the $M \times \langle Z \rangle$ bins.

dominance of phase space [35,43]. Indeed both dynamical and statistical approaches were able to reproduce the experimental observation. With the same dynamical approach as that used in this paper, the experimental charge and multiplicities distributions were reproduced, while the average fragment kinetic energies were accounted for within 20% [7]. These same properties were also well accounted for with the statistical model SMM [43–46]. From this agreement between data and the two models we learnt that the dynamics involved is sufficiently chaotic to finally explore enough of the phase space and describe fragment production through a statistical approach. To go further more constrained observables were needed. Such was the goal of the present studies.

We have just seen that, at 32 AMeV incident energy, experimental correlation functions are similar to those obtained with events from dynamical simulations, BOB. Above all, in both of them, there is abnormal production of nearly equal-sized fragments pointed out by the peaks in the first σ_Z bin(s). Supported by this simulation we thus attributed the greatest part of fusion-multifragmentation events to spinodal decomposition [17]. These peaks hence appear as fossil fingerprints of the break-up process.

Correlation peaks are also observed for experimental data at higher incident energies: the excitation function is displayed in fig. 10. Information on the associated thermal excitation energies (and extra radial collective energy) involved over the incident energy domain studied can be provided by the SMM model which well describes static and dynamics observables of fragments. Starting from a freeze-out volume fixed at three times the normal volume, the thermal excitation energies of the dilute and homogeneous system, extracted from SMM, vary from 5.0 to 7.0 AMeV and the added radial expansion energy remains low: from 0.5 to 2.2 AMeV [44,47]. A rise and fall of the percentage of "fossil partitions" from spinodal decomposition is measured. Figure 10 reveals some difference between the experimental (full symbols) and simulated (open symbols) events: the experimental percentages of extra events are closer to the simulated ones in fig. 10b than in fig. 10a. This means that the charge distributions inside an event are slightly narrower in the simulation than in the experiment either because of the primary intrinsic spread, or because the width due to evaporation is underestimated. For the considered system, incident energies around 35–40 AMeV appear as the most favourable to induce spinodal decomposition; it corresponds to about 5.5–6 AMeV thermal excitation energy associated to a very gentle expansion energy around 0.5–1 AMeV. The qualitative explanation for those numbers can be well understood in terms of a necessary compromise between two times. On the one hand, the fused systems have to stay in the spinodal region $\approx$ 100–150 fm/c [16,48,49], to allow an important amplification of the initial fluctuations and thus permit spinodal decomposition; this requires a not too high incident energy, high enough however for multifragmentation to occur. On the other hand, for a finite system, Coulomb interaction and collective expansion push the "primitive" fragments apart and reduce the time of their mutual interaction, which is efficient to keep a memory of "primitive" size properties. Above 45 AMeV incident energy part of trajectories followed by the system in the temperature-density plane may not sufficiently penetrate the spinodal region. Finally, considering secondary decay

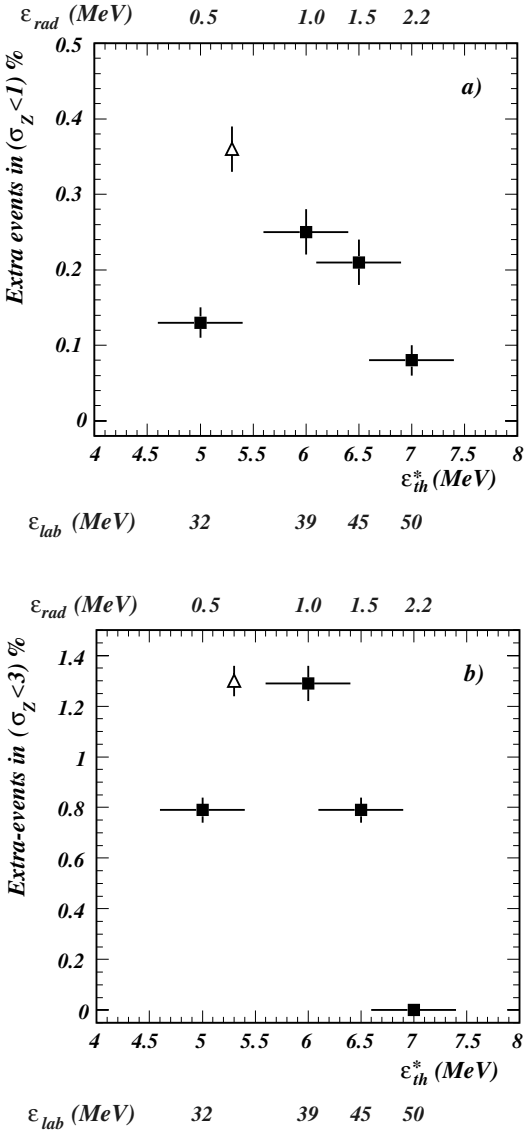

Fig. 10. Abnormal production of events with nearly equal-sized fragments (a: $\sigma_Z < 1$ and b: $\sigma_Z < 3$) as a function of thermal excitation energy (deduced from SMM): full points. The incident and radial energy scales are also indicated. The open point refers to the result from BOB simulations; the average thermal excitation energy is used. Vertical bars correspond to statistical errors and horizontal bars refer to estimated uncertainties on the backtraced quantity, ϵ^*.

effects, they should be essentially similar between 39 and 50 AMeV because the primary fragment excitation energy per nucleon was found constant over this incident energy range [27]. Particularly the excitation function shown in fig. 10 should not be affected by such effects.

Let us come now to the size of fragments associated to "fossil partitions". From the theoretical point of view, spinodal instabilities have been mainly studied within semiclassical (as BOB) or hydrodynamical [49–51] frameworks. Precise information on the most unstable collective modes, which is needed for discussing fragment size produced by spinodal decomposition, can only be obtained when considering quantal effects. From the limited number of studies investigating such effects [14,52,53] a few trends emerge: i) an increase of the number of unstable collective modes with the size of the system (up to multipolarity $L = 5$–6 for $A = 140$), ii) a decrease of the $L_{\max}$ value when the temperature increases and iii) a dominance of the octupole mode ($L = 3$) which appears as the most unstable. Charge correlations were only studied for events with 3 to 6 fragments, which precludes any information on the quadrupole mode ($L = 2$). If we except results at the highest incident energy, which strongly differ from others, we do observe the dominance of events with three fragments, associated to the multipolarity $L = 3$. Indeed the Z domains marked in bold in table 2 correspond to the largest proportion of events which populate the first σ_Z bin, which vary from 70% at 32 AMeV to 40% at 45 AMeV. Then the number of events with higher multiplicities, corresponding to larger L values, progressively decreases, as expected.

At 50 AMeV results observed for the fragment sizes ($\sigma_Z < 1$) are puzzling. Moreover, the percentage of extra events drops to zero when events with $\sigma_Z < 3$ are considered. Further simulations and theoretical works are needed to progress in the interpretation of these data.

6 Conclusions

In conclusion, we have investigated charge correlation functions for compact and heavy fused systems which undergo multifragmentation, as a function of the incident energy, from 32 to 50 AMeV. At the lowest energy, we have confirmed an enhanced production of events with equal-sized fragments. Supported by theoretical simulations we have interpreted this enhancement as a signature of spinodal instabilities as the origin of multifragmentation of those systems in the Fermi energy domain. This fossil signal culminates for incident energy around 35–40 AMeV, which corresponds to the formation of a hot and dilute system at 0.3–0.4 the normal density and temperature around 4–5 MeV [54,7]. Spinodal decomposition describes the dynamics of a first-order phase transition, and the present observations support the existence of such a transition for hot finite nuclear matter [3,45,9].

The experimental results were obtained by the INDRA Collaboration.

Appendix

Very recently, a new method for building charge correlation functions was proposed, of implementation easier than the IPM method: the denominator is built by mixing events through random exchanges of two fragments between two events under the constraint that the sum of the two exchanged fragments is conserved, besides the conservation of $Z_{\rm bound}$ [36]. To test the sensitivity of this

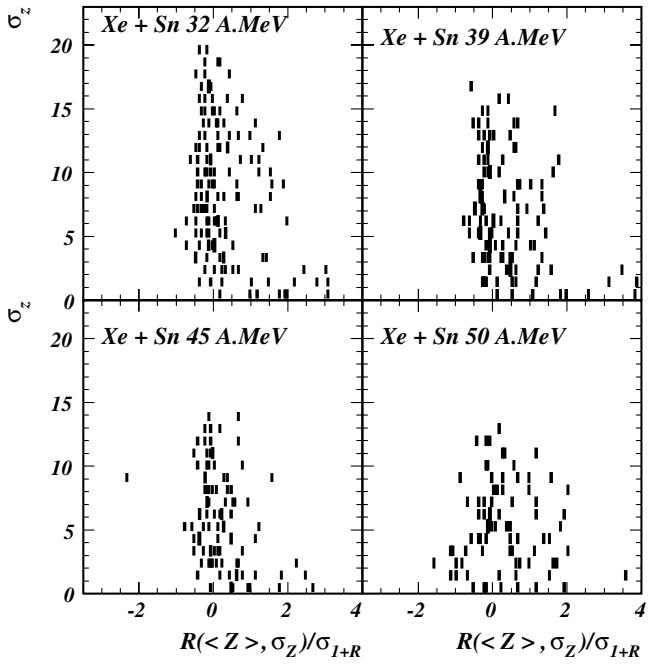

Fig. 11. Deviations from 1 of the correlation functions divided by the statistical errors in abcissa, for the different values of σ_Z. Correlation functions calculated by the IPM method, and shown in fig 7.

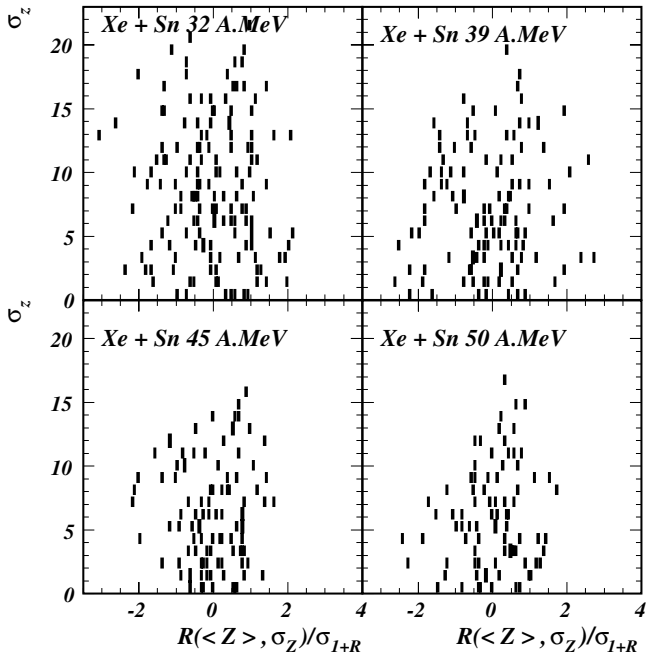

Fig. 12. Deviations from 1 of the correlation functions divided by the statistical errors in abcissa, for the different values of σ_Z. Correlation functions calculated by the exchange mixing event method.

method as compared to the IPM method, the present experimental data were also analyzed using the exchange method, by building correlation functions $1 + R(\sigma_Z, \langle Z\rangle)$ with σ_Z being calculated from eq. (2). The results of the two methods are compared in fig. 11 and fig. 12, displaying for each bin of the plane (σ_Z, $M \times \langle Z\rangle$), the deviation from 1, $R(\sigma_Z, \langle Z\rangle)$, of the correlation function, normalized to its statistical error bar, $\sigma_{1+R(\sigma_Z,\langle Z\rangle)}$, calculated from the numerator only.

The greater sensitivity of the IPM method is clearly seen in fig. 11: the values of the correlation function are closer to one ($R = 0$) except at low σ_Z where we observe correlations with a significant confidence level. Conversely, the exchange method, fig. 12, leads to a large dispersion of the values of $R(\sigma_Z, \langle Z\rangle)/\sigma_{1+R(\sigma_Z,\langle Z\rangle)}$, ~ 1.6 times broader than with the IPM method at 32, 39 and 45 AMeV. At 50 AMeV both methods lead to similar dispersions.

References

1. L.G. Moretto, G.J. Wozniak, Annu. Rev. Nucl. Part. Sci. **43**, 379 (1993).
2. D.H.E. Gross, Rep. Prog. Phys. **53**, 605 (1990).
3. M. D'Agostino, F. Gulminelli, P. Chomaz, M. Bruno, F. Cannata *et al.*, Phys. Lett. B **473**, 219 (2000).
4. EOS Collaboration (J.A. Hauger *et al.*), Phys. Rev. C **62**, 024616 (2000).
5. EOS Collaboration (J.B. Elliott *et al.*), Phys. Rev. C **62**, 064603 (2000).
6. H. Xu *et al.*, Phys. Rev. Lett. **85**, 716 (2000).
7. INDRA Collaboration (J.D. Frankland, B. Borderie, M. Colonna, M.F. Rivet, C.O. Bacri *et al.*), Nucl. Phys. A **689**, 940 (2001).
8. R. Botet, M. Płoszajczak, A. Chbihi, B. Borderie, D. Durand *et al.*, Phys. Rev. Lett. **86**, 3514 (2001).
9. M. D'Agostino, R. Bougault, F. Gulminelli, M. Bruno, F. Cannata *et al.*, Nucl. Phys. A **699**, 795 (2002).
10. A.H. Raduta, A.R. Raduta, Phys. Rev. C **65**, 054610 (2002).
11. M. Kleine Berkenbrusch, W. Bauer, K. Dillman, S. Pratt, L. Beaulieu *et al.*, Phys. Rev. Lett. **88**, 022701 (2002).
12. J.B. Elliott, L.G. Moretto, L. Phair, G.J. Wozniak, L. Beaulieu *et al.*, Phys. Rev. Lett. **88**, 042701 (2002).
13. G.F. Bertsch, P.J. Siemens, Phys. Lett. B **126**, 9 (1983).
14. S. Ayik, M. Colonna, P. Chomaz, Phys. Lett. B **353**, 417 (1995).
15. B. Jacquot, S. Ayik, P. Chomaz, M. Colonna, Phys. Lett. B **383**, 247 (1996).
16. M. Colonna, P. Chomaz, A. Guarnera, Nucl. Phys. A **613**, 165 (1997).
17. INDRA Collaboration (B. Borderie, G. Tăbăcaru, P. Chomaz, M. Colonna, A. Guarnera *et al.*), Phys. Rev. Lett. **86**, 3252 (2001).
18. P. Désesquelles, Phys. Rev. C **65**, 034604 (2002).
19. INDRA Collaboration (J.D. Frankland, C.O. Bacri, B. Borderie, M.F. Rivet, M. Squalli *et al.*), Nucl. Phys. A **689**, 905 (2001).
20. J. Pouthas, B. Borderie, R. Dayras, E. Plagnol, M.F. Rivet *et al.*, Nucl. Instrum. Methods Phys. Res. A **357**, 418 (1995).
21. J. Pouthas, A. Bertaut, B. Borderie, P. Bourgault, B. Cahan *et al.*, Nucl. Instrum. Methods Phys. Res. A **369**, 222 (1996).
22. INDRA Collaboration (M. Pârlog, B. Borderie, M.F. Rivet, G. Tăbăcaru, A. Chbihi *et al.*), Nucl. Instrum. Methods Phys. Res. A **482**, 674 (2002).

23. INDRA Collaboration (M. Pârlog, B. Borderie, M.F. Rivet, G. Tăbăcaru, A. Chbihi *et al.*), Nucl. Instrum. Methods Phys. Res. A **482**, 693 (2002).
24. D. Cugnon, D. L'Hôte, Nucl. Phys. A **397**, 519 (1983).
25. J.F. Lecolley, L. Stugge, M. Aboufirassi, A. Badala, B. Bilwes *et al.*, Phys. Lett. B **325**, 317 (1994).
26. INDRA Collaboration (N. Marie, R. Laforest, R. Bougault, J.P. Wieleczko, D. Durand *et al.*), Phys. Lett. B **391**, 15 (1997).
27. INDRA Collaboration (S. Hudan, A. Chbihi, J.D. Frankland, A. Mignon, A. Botvina *et al.*), Phys. Rev. C **67**, 064613 (2003).
28. Anh-Dung Nguyen, thèse de doctorat, Université de Caen (1998), LPCC T 98-02.
29. G. Tăbăcaru, thèse de doctorat, Université Paris-XI Orsay (2000), IPNO T 00-13.
30. INDRA Collaboration (N. Marie, A. Chbihi, J. Natowitz, A. Le Fèvre, S. Salou *et al.*), Phys. Rev. C **58**, 256 (1998).
31. INDRA Collaboration (N. Bellaize, O. Lopez, J.P. Wieleczko, D. Cussol, G. Auger *et al.*), Nucl. Phys. A **709**, 367 (2002).
32. D. Sisan, W. Bauer, O. Bjarki, D.J. Magestro, A. Nadasen *et al.*, Phys. Rev. C **63**, 027602 (2001).
33. C. Williams, W.G. Lynch, C. Schwarz, M.B. Tsang, W.C. Hsi *et al.*, Phys. Rev. C **55**, 2132 (1997).
34. L.G. Moretto, T. Rubehn, L. Phair, N. Colonna, G.J. Wozniak *et al.*, Phys. Rev. Lett. **77**, 2634 (1996).
35. L.G. Moretto, R. Ghetti, L. Phair, K. Tso, G.J. Wozniak, Phys. Rep. **287**, 249 (1997).
36. J.L. Charvet, R. Dayras, D. Durand, O. Lopez, L. Nalpas *et al.*, to be published, nucl-ex/0212012.
37. J. Randrup, B. Remaud, Nucl. Phys. A **514**, 339 (1990).
38. P. Chomaz, G.F. Burgio, J. Randrup, Phys. Lett. B **254**, 340 (1991).
39. G.F. Burgio, P. Chomaz, J. Randrup, Nucl. Phys. A **529**, 157 (1991).
40. P. Chomaz, M. Colonna, A. Guarnera, J. Randrup, Phys. Rev. Lett. **73**, 3512 (1994).
41. A. Guarnera, P. Chomaz, M. Colonna, J. Randrup, Phys. Lett. B **403**, 191 (1997).
42. INDRA Collaboration (M.F. Rivet, C.O. Bacri, B. Borderie, J.D. Frankland, M. Assenard *et al.*), Phys. Lett. B **430**, 217 (1998).
43. J. Bondorf, A.S. Botvina, A.S. Iljinov, I.N. Mishustin, K. Sneppen, Phys. Rep. **257**, 133 (1995).
44. S. Salou, thèse de doctorat, Université de Caen (1997), GANIL T 97 06.
45. INDRA Collaboration (N. Le Neindre *et al.*), *Proceedings of the International Conference on Structure of the Nucleus at the Dawn of the Century, Bologna, Italy, Nucleus-Nucleus Collisions*, edited by G. Bonsignori, M. Bruno, A. Ventura, D. Vretenar, Vol. **1** (World Scientific, Singapore, 2001) p. 221.
46. INDRA Collaboration (G. Tăbăcaru *et al.*), *Proceedings of the International Conference on Structure of the Nucleus at the Dawn of the Century, Bologna, Italy, Nucleus-Nucleus Collisions*, edited by G. Bonsignori, M. Bruno, A. Ventura, D. Vretenar, Vol. **1** (World Scientific, Singapore, 2001) p. 321.
47. N. Le Neindre, thèse de doctorat, Université de Caen (1999), LPCC T 99 02.
48. D. Idier, M. Farine, B. Remaud, F. Sébille, Ann. Phys. (Paris) **19**, 159 (1994).
49. W. Nörenberg, G. Papp, P. Rozmej, Eur. Phys. J. A **14**, 43 (2002).
50. W. Nörenberg, G. Papp, P. Rozmej, Eur. Phys. J. A **9**, 327 (2000).
51. H. Heiselberg, C.J. Pethick, D.G. Ravenhall, Phys. Rev. Lett. **61**, 818 (1988).
52. P. Chomaz, D. Lacroix, B. Jacquot, M. Colonna, S. Ayik, *Proceedings of the XXVII International Workshop on Gross properties of Nuclei and Nuclear Excitations, Hirschegg, Austria*, edited by H. Feldmeier, J. Knoll, W. Nörenberg, J. Wambach (GSI, Darmstadt, 1999) p. 312.
53. M. Colonna, P. Chomaz, S. Ayik, Phys. Rev. Lett. **88**, 122701 (2002).
54. A. Guarnera, thèse de doctorat, Université de Caen (1996), GANIL T 96 01.